International Journal of Heat and Mass Transfer 52 (2009) 2792–2801

Contents lists available at ScienceDirect

International Journal of Heat and Mass Transfer

journal homepage: www.elsevier.com/locate/ijhmt

# An evaluation of secondary effects on microchannel frictional and convective heat transfer characteristics

J. van Rij, T. Ameel *, T. Harman

*Department of Mechanical Engineering, University of Utah, Salt Lake City, UT 84112, USA*

ARTICLE INFO

*Article history:*
Received 28 May 2008
Received in revised form 4 December 2008
Available online 11 February 2009

*Keywords:*
Rarified flow
Viscous dissipation
Axial conduction

ABSTRACT

The frictional and convective heat transfer characteristics of rarified flows in rectangular microchannels, with either isoflux or isothermal boundary conditions, are evaluated subject to second-order slip boundary conditions, creep flow, viscous dissipation, and axial conduction effects. Numerical results are obtained using a continuum based, three-dimensional, compressible, unsteady computational fluid dynamics algorithm with first- and second-order slip velocity and temperature jump boundary conditions applied to the momentum and energy equations, respectively. The results, reported in the form of Poiseuille and Nusselt numbers, are found to be significant functions of aspect ratio, Knudsen number, slip model parameters, Brinkman number, and Peclet number.



## 1. Introduction

The heat transfer and friction losses of steady state gaseous flows in microchannels are important due to their applications in microscale heat exchangers, sensors, reactors, power systems, etc. For this reason, there have been numerous studies on slip flow frictional losses and convective heat transfer for constant wall temperature and constant wall heat flux boundary conditions within parallel plate, cylindrical, rectangular, and trapezoidal microchannels. Because conventional micro fabrication methods often produce planar and rectangular channel geometries, an accurate evaluation and understanding of the flow and heat transfer characteristics for rectangular microchannels is particularly important. The majority of previous studies have been analytical, although there are also several numerical studies based on either statistical or continuum methods. Nearly all theoretical studies have assumed first-order accurate slip velocity and temperature jump boundary conditions, laminar, steady state, hydrodynamically fully developed, constant property flow with negligible creep flow, viscous dissipation, and axial conduction effects. However, the accuracy of these simplifications, and consequently the results of these studies, have not yet been verified numerically or experimentally.

There are several factors that cause microscale fluid systems to behave differently than standard macroscale fluid systems. For micro systems with gaseous flows, rarefaction effects may be considerable. Rarefaction takes place as either the size or the pressure of a fluid system decreases, resulting in a mean free path of the fluid molecules that is comparable to the characteristic length of the system itself. When this occurs, discontinuities between the fluid and the solid surface, as well as other noncontinuum behaviors begin to develop. Typically, the Knudsen number, $Kn$, is used to represent the degree of rarefaction, or noncontinuum effects present. The Knudsen number is defined as the ratio of the fluid's molecular mean free path to the characteristic length of the flow. Empirically, the Knudsen number has been used to classify flows into four different regimes [1]. While in the continuum flow regime ($Kn \leqslant 0.01$), conventional continuum conservation of momentum and energy methods, such as the Navier–Stokes equations, may be used. For the free molecular flow regime ($Kn \geqslant 10$), free molecular models such as the Boltzmann equation must be solved. In the transition flow regime ($0.1 \leqslant Kn \leqslant 10$), either numerical solutions of the Boltzmann equation or direct-simulation-Monte-Carlo (DSMC) methods are commonly used. For the slip flow regime ($0.01 \leqslant Kn \leqslant 0.1$), it has been determined experimentally that the deviation of molecular motion from the continuum distribution is small enough that models based on the continuum equations may be used, but with 'slip velocity' and 'temperature jump' boundary conditions that take into account the incomplete momentum and energy exchange between the fluid molecules and the solid surface.

The original slip velocity boundary condition, given in Eq. (1), and temperature jump boundary condition, given in Eq. (2), were derived by Maxwell [2] and Smoluchowski [3], respectively.

$$u|_{y=0} - u_w = \left[\left(\frac{2-\sigma_v}{\sigma_v}\right)\frac{\lambda}{\mu}\tau + \frac{3}{4}\frac{\mu R}{P}\frac{\partial T}{\partial x}\right]_{y=0} \tag{1}$$

$$T|_{y=0} - T_w = \left[\left(\frac{2-\sigma_t}{\sigma_t}\right)\left(\frac{2\gamma}{1+\gamma}\right)\frac{\lambda}{Pr}\frac{\partial T}{\partial y}\right]_{y=0} \tag{2}$$

* Corresponding author. Tel.: +1 801 585 9730; fax: +1 801 585 9826.
*E-mail address:* ameel@mech.utah.edu (T. Ameel).

0017-9310/$ - see front matter © 2009 Elsevier Ltd. All rights reserved.
doi:10.1016/j.ijheatmasstransfer.2009.01.001

**Nomenclature**

| | |
|---|---|
| $AR$ | aspect ratio, $b/h$ |
| $b$ | one-half the channel width |
| $Br$ | Brinkman number, $Br_{H2} = \mu u_m^2/(q_w D_h)$, $Br_T = \mu u_m^2/(k(T_i - T_w))$ |
| $c_p$ | specific heat at constant pressure |
| $c_v$ | specific heat at constant volume |
| $D_h$ | hydraulic diameter, $4hb/(h+b)$ |
| $f$ | friction factor, $8\tau_{w,m}/(\rho u_m^2)$ |
| $h$ | one-half the channel height |
| $k$ | thermal conductivity |
| $Kn$ | Knudsen number, $\lambda/D_h$ |
| $L$ | channel length |
| $Ma$ | Mach number, $(PeKn/\mathrm{Pr})\sqrt{2/(\pi\gamma)}$ |
| $Nu$ | Nusselt number, $q_{w,m}D_h/(k(T_w - T_m))$ |
| $Pe$ | Peclet number, $Pr\,Re$ |
| $Po$ | Poiseuille number, $f\,Re$ |
| $Pr$ | Prandtl number, $c_p\mu/k$ |
| $q$ | heat flux |
| $R$ | gas constant |
| $Re$ | Reynolds number, $\rho u_m D_h/\mu$ |
| $T$ | temperature |
| $u$ | streamwise velocity |
| $u_c$ | creep velocity, $(3/4)(\mu R/P)(\partial T/\partial x)\|_{y=0}$ |
| $x, y, z$ | Cartesian coordinates |

*Greek symbols*

| | |
|---|---|
| $\beta$ | gas–wall interaction parameter, $\beta_{t1}/\beta_{v1}$ |
| $\beta_{t1}$ | first-order temperature jump coefficient, $((2-\sigma_t)/\sigma_t)(2\gamma/(1+\gamma))(1/Pr)$ |
| $\beta_{t2}$ | second-order temperature jump coefficient |
| $\beta_{v1}$ | first-order velocity slip coefficient, $(2-\sigma_v)/\sigma_v$ |
| $\beta_{v2}$ | second-order velocity slip coefficient |
| $\beta_{v1}Kn$ | rarefaction parameter |
| $\varepsilon$ | relative error |
| $\gamma$ | ratio of specific heat capacities, $c_p/c_v$ |
| $\lambda$ | molecular mean free path, $\mu/(\rho\sqrt{2RT/\pi})$ |
| $\mu$ | dynamic viscosity |
| $\rho$ | density |
| $\sigma_t$ | thermal accommodation coefficient |
| $\sigma_v$ | momentum accommodation coefficient |
| $\tau$ | shear stress |

*Subscripts*

| | |
|---|---|
| $H2$ | constant wall heat flux condition |
| $i$ | inlet value |
| $m$ | mean value |
| $o$ | nominal continuum value |
| $T$ | constant wall temperature condition |
| $w$ | wall value |

Eqs. (1) and (2), as well as subsequent equations, are presented in a format assuming a Cartesian coordinate system, a wall normal direction ($y$), and a streamwise direction ($x$). The first term in Eq. (1) is the slip velocity due to the shear stress at the wall, and the second term is the thermal creep velocity, $u_c$, due to a temperature gradient tangential to the wall. Values for the momentum accommodation coefficient, $\sigma_v$, and the thermal accommodation coefficient, $\sigma_t$, range from zero to one, where $\sigma_v = 0$ represents completely specular reflection, $\sigma_v = 1$, represents completely diffuse reflection, and $\sigma_t = 1$ corresponds to a perfect energy exchange.

Eqs. (1) and (2) are a result of a first-order expansion, in $Kn$, of the Boltzmann equation, and understood to be applicable only in the slip flow regime. However, in an effort to extend the range of applicability of slip flow boundary conditions to higher Knudsen number flows, specifically the transition regime, many 'second-order' modifications and methods have been proposed [1,4–9]. The boundary conditions derived by Deissler [4], given in Eqs. (3) and (4), and the boundary conditions suggested by Karniadakis and Beskok [1], given in Eqs. (5) and (6), are two of the more commonly applied second-order slip boundary condition models, as well as the only prevalent second-order models that provide temperature as well as velocity boundary conditions.

$$u|_{y=0} - u_w = \left[\left(\frac{2-\sigma_v}{\sigma_v}\right)\lambda\frac{\partial u}{\partial y} - \frac{9}{16}\lambda^2\left(2\frac{\partial^2 u}{\partial y^2} + \frac{\partial^2 u}{\partial x^2} + \frac{\partial^2 u}{\partial z^2}\right)\right]_{y=0} \tag{3}$$

$$T|_{y=0} - T_w = \left[\left(\frac{2-\sigma_t}{\sigma_t}\right)\left(\frac{2\gamma}{1+\gamma}\right)\frac{\lambda}{\mathrm{Pr}}\frac{\partial T}{\partial y} - \frac{9\lambda^2}{256}\left(\frac{177\gamma - 145}{\gamma+1}\right) \times \left(2\frac{\partial^2 T}{\partial y^2} + \frac{\partial^2 T}{\partial x^2} + \frac{\partial^2 T}{\partial z^2}\right)\right]_{y=0} \tag{4}$$

$$u|_{y=0} - u_w = \left(\frac{2-\sigma_v}{\sigma_v}\right)\left[\lambda\frac{\partial u}{\partial y} + \frac{\lambda^2}{2}\frac{\partial^2 u}{\partial y^2}\right]_{y=0} \tag{5}$$

$$T|_{y=0} - T_w = \left(\frac{2-\sigma_t}{\sigma_t}\right)\left(\frac{2\gamma}{1+\gamma}\right)\frac{1}{\mathrm{Pr}}\left[\lambda\frac{\partial T}{\partial y} + \frac{\lambda^2}{2}\frac{\partial^2 T}{\partial y^2}\right]_{y=0} \tag{6}$$

Although many second-order models have been proposed, and some have proven useful in increasing the range and accuracy of the slip boundary condition representation of rarefaction, either experimentally [10,11], or numerically [1], there is currently insufficient experimental data to validate the use of any particular second-order model over another. Nonetheless, as additional experimental and theoretical results become available, convective heat transfer solutions with second-order terms may prove useful. Presently, however, there are few analytical or numerical convective heat transfer solutions based on second-order slip boundary condition models [1,4,12–17], and these are often presented for limited values of Knudsen number, momentum and thermal accommodation coefficients, geometry, etc., and consequently have limited applicability.

In addition to rarefaction effects, there are other effects that are often a result of 'scaling.' Scaling effects are not unique to micro flows, but where in a macro system they are typically negligible, in a micro system they become more prominent and may even dominate the flow characteristics. Many of the scaling effects in micro fluidic systems are a consequence of the increased surface area to volume ratio. This results in increased surface forces, which may produce large pressure drops, compressibility effects, and viscous dissipation; decreased inertial forces, which allows diffusion and conduction processes to become relatively more significant; and increased heat transfer, which may lead to variable fluid properties and creep flow.

While creep flow is typically negligible for large scale flows and fully developed, constant wall temperature flows, creep flow effects may become significant for constant wall heat flux flows within the slip regime. The effect of creep flow has been shown to significantly alter the pressure losses and convective heat transfer rates from that predicted when creep flow is neglected for several geometries [13,16,17]. However, the effect of creep flow on fully developed, constant wall heat flux, rectangular microchannel pressure losses and convective heat transfer rates, calculated in conjunction with slip velocity and temperature jump boundary conditions, has not yet been examined.

In macroscale systems, viscous dissipation effects are only significant for high velocity or highly viscous flows. However, in microscale systems large channel length to hydraulic diameter ratios result in large velocity and pressure gradients, and consequently thermal energy generation due to viscous dissipation. A slight increase in fluid temperature may be significant relative to the small temperature gradients typically present in microchannels, and as a result alter the convective heat transfer rate and any temperature dependant fluid properties, particularly viscosity, which further changes the convective heat transfer rate, as well as the frictional losses. Because the function of many micro fluidic systems is cooling, viscous dissipation becomes a limiting factor that must be accurately represented. Effects of viscous dissipation are characterized by the Brinkman number, *Br*, where $Br \approx 0$ indicates that viscous dissipation effects are negligible. Recently, several studies have focused specifically on viscous dissipation effects for slip flow convective heat transfer [18–26]. However, most of these studies evaluated the effect of viscous dissipation without also evaluating the effects of flow work and shear work, which for gaseous flows are of the same order of magnitude as viscous dissipation; and, viscous dissipation effects in rectangular microchannels with constant wall temperature (*T*) and constant wall heat flux (*H*2) thermal boundary conditions have not yet been evaluated.

The significance of streamwise conduction is generally established by the magnitude of the flow Peclet number. The Peclet number, *Pe*, represents the ratio of the thermal energy convected to the fluid, to the thermal energy axially conducted within the fluid. A low *Pe*, which is common for micro flows, generally indicates that streamwise conduction effects must be considered. Previous studies have established correlations for the convective heat transfer rate for both continuum and slip flows in parallel plate and circular duct channels with *Pe* as a parameter [25,27–30]. However, axial conduction effects have been neglected in studies on rectangular channel, constant wall temperature flows, and consequently there is an absence of *Nu* data for fully developed conditions at low *Pe* in both the continuum and slip flow regimes.

Based on the preceding review, it is evident that theoretical results for microchannel frictional and convective heat transfer characteristics are generally obtained assuming first-order accurate slip boundary conditions, while second-order slip boundary conditions, creep flow, viscous dissipation, and axial conduction are considered negligible secondary effects. However, the accuracy of these assumptions, and consequently the results of these studies, have not yet been verified numerically or experimentally. The intent of this study is to numerically evaluate the significance of second-order slip boundary conditions, creep flow, viscous dissipation, and axial conduction on the convective heat transfer rate and frictional losses of steady state, laminar, nearly incompressible, locally fully developed, constant wall temperature (*T*) and constant wall heat flux (*H*2) rectangular microchannel flows in the slip flow regime.

## 2. Numerical algorithm

The computational fluid dynamics (CFD) algorithm used for this study has been described, and verified in previous microchannel investigations [17,31–33]. The algorithm is based on ICE (Implicit, Continuous-fluid Eulerian), which is a finite volume, multi-material CFD method. The ICE implementation used in this study is well developed and documented [34–37]. The code is three-dimensional, fully compressible, unsteady, and capable of modeling variable fluid properties, fluid–structure interactions, and chemical reactions. To accurately model microchannel flows, the algorithm has been modified to model any of the first- or second-order slip boundary conditions models presented in Eqs. (1)–(6), creep flow, and viscous dissipation. Slip velocity, temperature jump, creep flow, and viscous dissipation effects may be either included or neglected with each computation. The implementation of these modifications is consistent with the original code in being numerically second-order accurate both spatially and temporally.

Numerical results are obtained for the three-dimensional, continuum, momentum and energy equations with both first- and second-order slip velocity and temperature jump boundary conditions for the flow configuration illustrated in Fig. 1. The flow is modeled assuming laminar flow of a Newtonian, ideal gas, with constant properties ($c_p$, $k$, $\mu$) of air. To decrease the computational time required to reach a solution, only one quarter of the symmetric microchannel is modeled. The resulting velocity field is then evaluated to obtain the Poiseuille number, *Po*, which is an indication of the pressure drop characteristics and the temperature field is evaluated to obtain the Nusselt number, *Nu*, which represents the convective heat transfer characteristics.

### 2.1. Solution criteria

For the numerical solutions to be comparable to previous first-order analytic solutions, the flow must be nearly incompressible. To achieve this criterion, a low Mach number, $Ma = (PeKn/\mathrm{Pr})\sqrt{2/(\pi\gamma)}$, is maintained, generally 0.05 or less. For these low *Pe* flows, a channel length of $12h$ is found to be sufficient for *Po* and *Nu* values to become locally fully developed while avoiding significant compressibility effects due to a longer channel. For all cases, a uniform inlet velocity and temperature are specified while the outlet temperature and velocity profiles are allowed to evolve to their locally fully developed profiles. The inlet velocity, inlet temperature, outlet pressure, and wall temperature or wall heat flux are specified to obtain the intended flow *Pe*, $u_c/u_m$, $Br_{H2}$ or $Br_T$, and *Kn*.

Because the algorithm is unsteady, all of the flow properties must evolve from a set of initial values to steady state conditions subject to the boundary conditions. The initial velocity field is zero and the initial temperature field is equal to the inlet temperature. The convergence criterion for each time step is a mass flux residual less than $10^{-9}$ for each control volume. The criterion used to establish that the flow is steady state is $|(u^{n+1} - u^n)/u^{n+1}| \leqslant 10^{-10}$ and $|(T^{n+1} - T^n)/T^{n+1}| \leqslant 10^{-10}$, for each control volume, where $n$ is the number of the time step. The magnitude and number of time steps required to reach steady state are dependent on the grid resolution, $\beta_{v1}Kn$, and *Pe*.

### 2.2. Grid convergence and code verification

To assure that each numerical result is sufficiently accurate and converges to a grid independent solution, grid resolution studies have been completed for each *Po* and *Nu* reported. Table 1 presents the grid resolution studies for $Nu_{H2}$ with $\beta_{v1}Kn = 0$, and $AR = 1$, 2, and 5. For each aspect ratio, the relative change in $Nu_{H2}$ is less than 0.5% between the two highest grid resolutions. These data indicate that the numerical algorithm converges with approximately second-order numerical accuracy, and that the highest grid resolution

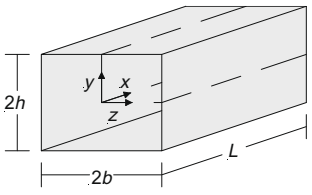


**Fig. 1.** Rectangular channel configuration.

**Table 1**
Grid resolution effects on rectangular channel, continuum flow $Nu_{H2}$, with comparison to analytic solutions.

| AR | Grid | $Nu_{H2}$, present | $Nu_{H2}$ [19] | $Nu_{H2}$ [27] | $Nu_{H2}$ [29] | $Nu_{H2}$ [38] |
|---|---|---|---|---|---|---|
| 1 | 10 × 10 × 120 | 3.175 | 3.10 | 3.09 | 3.135 | 3.091 |
| | 20 × 20 × 240 | 3.108 | | | | |
| | 40 × 40 × 480 | 3.092 | | | | |
| 2 | 10 × 20 × 120 | 3.070 | 3.03 | 3.02 | 3.065 | 3.022 |
| | 20 × 40 × 240 | 3.031 | | | | |
| | 40 × 80 × 480 | 3.022 | | | | |
| 5 | 10 × 50 × 120 | 2.964 | 2.90 | 2.93 | 2.961 | 2.922 |
| | 20 × 100 × 240 | 2.936 | | | | |
| | 40 × 200 × 480 | 2.929 | | | | |

tested for each *AR*, is sufficiently accurate when compared to the analytic solutions of [19,27,29,38]. Based on these data, all of the following results are obtained using the finest grid resolution given in Table 1.

The algorithm's ability to model first- and second-order velocity slip and temperature jump boundary conditions, as well as creep flow and viscous dissipation has been verified previously for two-dimensional flows with both constant wall heat flux and constant wall temperature boundary conditions [17,31]. Prior to conducting the current study, it must also be verified that the algorithm is capable of accurately modeling axial conduction effects, and three-dimensional, rectangular microchannel pressure losses and convective heat transfer with first-order slip boundary conditions. To establish that the algorithm is accurate in modeling axial conduction effects, numerical and analytical $Nu_T$ [29], as a function of *Pe*, for parallel plate continuum flow are compared in Table 2. These data indicate that the code accurately models axial conduction effects, with an average difference between numerically and analytically computed $Nu_T$ of 0.10%, and a maximum difference of 0.35%.

To verify that the algorithm accurately models first-order slip flow pressure losses in rectangular microchannels, numerically computed *Po*, for the parameters given in Fig. 2(a), are compared to the analytically computed values of [39]. The analytical and numerical *Po* in this comparison do not differ by more than 0.14% and, on average, by only 0.04%, thereby verifying that the algorithm is capable of modeling first-order slip flow pressure losses. To verify that the algorithm accurately models first-order convective heat transfer in rectangular microchannels, numerically computed $Nu_{H2}$, for the parameters given in Fig. 2(b), are compared to the analytically computed values of [19,29]. This comparison demonstrates that the numerically computed $Nu_{H2}$ values closely agree with the analytically computed values of [29], but the analytic values are an average of 1.26% higher. Although this discrepancy is minor, it may be noted that the values of [29], presented in Table 2 for continuum flow, are also slightly higher, 1.39% on average, than all other references [19,27,38]. The analytically computed values of [19] for *AR* = 1 are all within 0.5% of the present numerical data. At *AR* = 5, there are more significant differences, nearly

**Table 2**
Comparison of numerically and analytically computed $Nu_T$ for parallel plate, continuum flow with axial conduction.

| Pe | $Nu_T$, present | $Nu_T$ [29] | ε (%) |
|---|---|---|---|
| 0.005 | 8.117 | 8.119 | −0.02 |
| 0.05 | 8.111 | 8.111 | 0.00 |
| 0.5 | 8.050 | 8.058 | −0.10 |
| 5.0 | 7.720 | 7.747 | −0.35 |
| 50 | 7.563 | 7.562 | 0.01 |

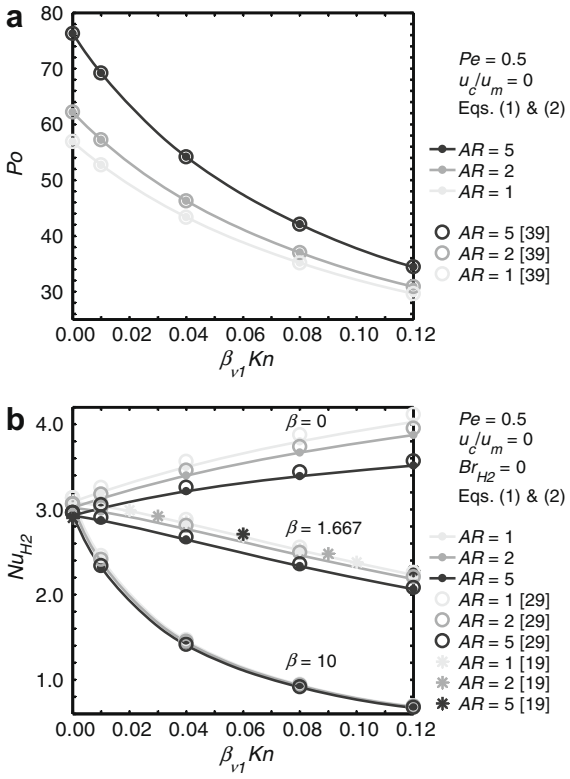


**Fig. 2.** Comparison of numerically and analytically computed: (a) *Po*, (b) $Nu_{H2}$.

10% in some cases, however, the predicted tends due to rarefaction, remain comparable. The excellent agreement of the present $Nu_{H2}$ data and the analytic data of [29], as well as the general agreement in trends of [19], indicates that the code is capable of accurately modeling first-order slip flow convective heat transfer rates for rectangular microchannels.

## 3. Results and discussion

An evaluation and summary of the effects of first- and second-order slip boundary condition models, creep flow, viscous dissipation, and axial conduction on rectangular microchannel pressure drop and convective heat transfer characteristics are presented in Figs. 3–8. All *Po* and *Nu* are normalized by nominal continuum values without creep flow, or viscous dissipation effects, $Po_o$ and $Nu_o$, respectively. All numerically computed values are specified by symbols, with the connecting lines representing the data trend. All other relevant flow parameters are indicated in the Figures.

### 3.1. Second-order slip boundary condition effects

Fully developed $Po/Po_o$, for the different slip flow boundary condition models, are presented in Fig. 3 for *AR* = 1, 2, 5, and ∞. The boundary conditions are first-order slip, Eqs. (1) and (2), second-order Deissler slip, Eqs. (3) and (4), and second-order Karniadakis and Beskok slip, Eqs. (5) and (6). For these data *Pe* = 0.5, *Br* = 0, and $u_c/u_m$ = 0. The data in Fig. 3 indicate that $Po/Po_o$ decreases with $\beta_{v1}Kn$ for all *AR*, and that the effect of *AR* on *Po* is significant in both the continuum and slip flow regimes. Within the continuum flow regime, $Po_o$ decreases from 96, for *AR* = ∞, to 56.9, for *AR* = 1, due to the reduced average wall shear stress caused by the proximity of the corners. Within the slip flow regime, increasing rarefaction, $\beta_{v1}Kn$, increases the slip velocity at the walls, which results in a flatter velocity profile with reduced wall velocity gradients and

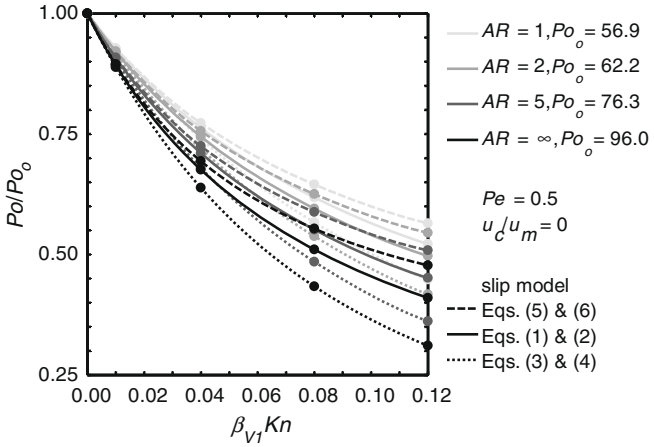


**Fig. 3.** Effect of second-order slip boundary conditions on fully developed $Po/Po_o$.

consequently reduces $Po/Po_o$ for all $AR$. Although $Po/Po_o$ decreases with $\beta_{v1}Kn$ for all $AR$, the slip velocity is a function of both $\beta_{v1}Kn$ and the average wall velocity gradients, which are larger for higher $AR$ flow, and as a result $Po/Po_o$ decreases more significantly for higher $AR$ flows.

The data in Fig. 3 also illustrate that second-order slip terms become more significant as $\beta_{v1}Kn$ increases. However, the two second-order models have opposite effects when compared to the first-order boundary condition data. This result is expected, due to the opposite signs of the second-order coefficients, given in Eqs. (3) and (5). As compared to the first-order boundary condition data, the second-order Deissler boundary conditions result in an increase in the slip velocity and consequently reduces $Po/Po_o$ with $\beta_{v1}Kn$, while the second-order Karniadakis and Beskok boundary conditions result in a decrease in the slip velocity and consequently increases $Po/Po_o$ with $\beta_{v1}Kn$. Second-order effects are more significant for larger $AR$ due, again, to the larger average wall velocity gradients.

Fully developed $Nu_{H2}$ and $Nu_T$ are presented in Fig. 4 for the same slip flow boundary condition models, $Pe$, $Br$, $u_c/u_m$, and $AR$ values as the $Po/Po_o$ data in Fig. 3. The data in Fig. 4 indicate that both $Nu_T$ and $Nu_{H2}$ may increase or decrease with $\beta_{v1}Kn$, depending on $\beta$, for all $AR$ investigated, and that the effect of $AR$ on $Nu_T$ is more significant in both the continuum and the slip flow regimes than it is for $Nu_{H2}$. Within the continuum flow regime, $Nu_T$ increases significantly from 3.36, at $AR = 1$, to 8.06, at $AR = \infty$ ($Pe = 0.5$). This is due to the varying wall heat flux, which is maximum at the midpoint of the longest side and zero at the corners, resulting in a lower average wall heat flux at lower $AR$. $Nu_{H2}$, however, is nearly constant with respect to $AR$ – it decreases approximately 6% from 3.09, at $AR = 1$, to 2.91, at $AR = 10$, and does not approach the $AR = \infty$ value of $Nu_{H2} = 8.235$ [27]. This behavior is due to the $H2$ boundary condition, for which the heat flux is constant both axially and peripherally (the nondimensional wall temperature is maximum at the corners and minimum at the midpoint of the long side), and as such the heat flux on the two side walls will always have an effect, even at large $AR$.

The data trends in Fig. 4 for the slip flow regime are related to the fact that as rarefaction, $\beta_{v1}Kn$, increases, both the slip velocity and the temperature jump at the wall increase, for $\beta \neq 0$. An increase in the slip velocity enhances the energy exchange near the wall, which tends to increase both $Nu_T$ and $Nu_{H2}$, as displayed when $\beta = 0$. However, for $\beta \neq 0$, increasing $\beta_{v1}Kn$ also increases the temperature jump, which reduces the energy exchange, increases the difference between the mixed mean fluid temperature and the wall temperature, and tends

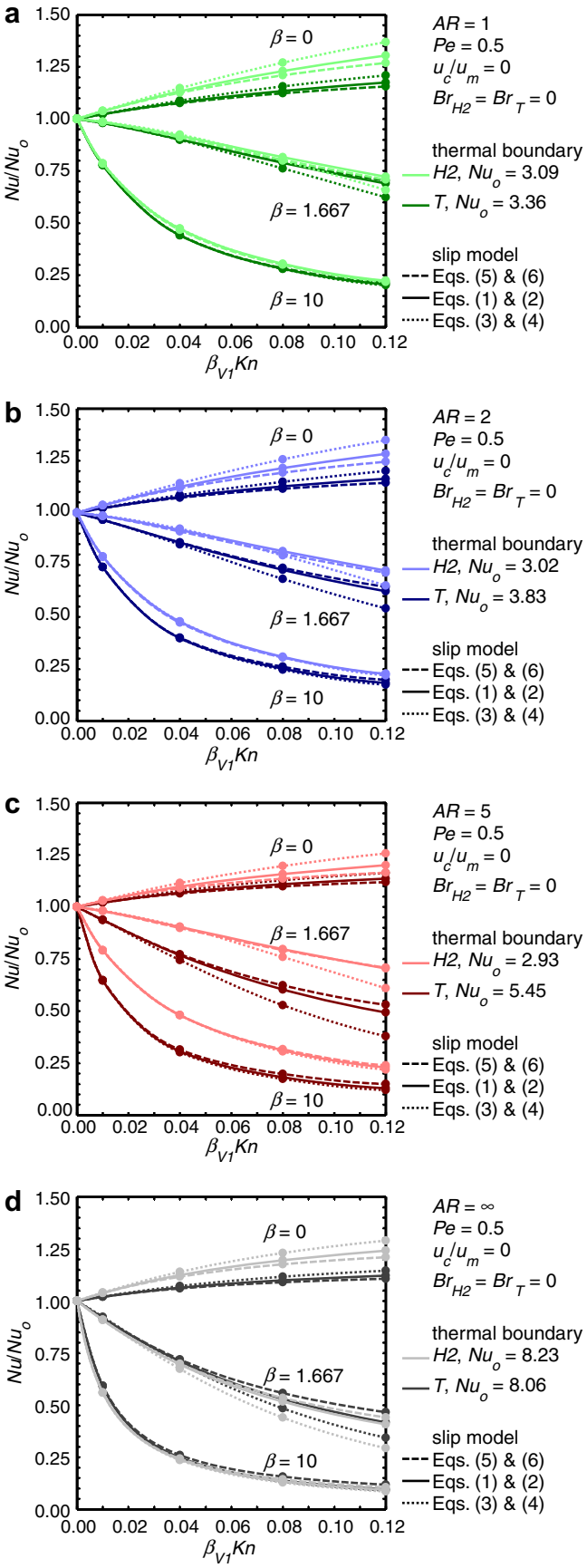


**Fig. 4.** Effect of second-order slip boundary conditions on fully developed $Nu/Nu_o$: (a) $AR = 1$, (b) $AR = 2$, (c) $AR = 5$, (d) $AR = \infty$.

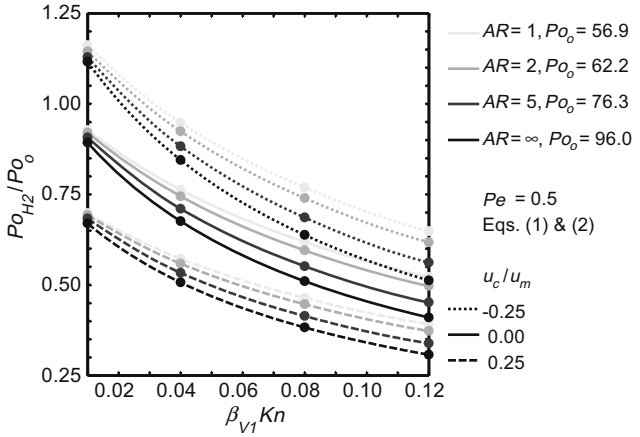


**Fig. 5.** Effect of creep flow on fully developed $Po_{H2}/Po_o$.

to decrease both $Nu_T$ and $Nu_{H2}$. While the wall heat flux is independent of $AR$ and $\beta_{v1}Kn$ for the $H2$ boundary condition, the average wall heat flux for the constant wall temperature boundary condition is reduced for both decreasing $AR$, and increasing $\beta_{v1}Kn$. These effects result in a less significant increase in $Nu_T$ due to slip, when $\beta = 0$, and a more significant decrease in $Nu_T$ with $\beta_{v1}Kn$, when $\beta \neq 0$, compared to $Nu_{H2}$.

The results in Fig. 4 also indicate that second-order temperature jump terms become more significant as $\beta_{v1}Kn$ increases. For the constant wall temperature boundary condition the average wall normal first-order and second-order temperature gradients are of opposite sign for all $AR$, $\beta$, and $\beta_{v1}Kn$ evaluated. When $\beta \neq 0$, this causes the second-order Deissler boundary conditions to predict an increase in the temperature jump (decrease in $Nu_T$), compared to the first-order boundary condition data; while the second-order Karniadakis and Beskok boundary conditions predict a decrease in the temperature jump (increase in $Nu_T$), compared to the first-order boundary conditions. For the constant wall heat flux boundary condition, the average wall normal first-order and second-order temperature gradients are of the same sign for lower $AR$ and $\beta_{v1}Kn$ values, and of opposite sign for increasing $AR$ and $\beta_{v1}Kn$ values. This causes the second-order Deissler boundary conditions to predict a decrease in temperature jump (increase in $Nu_{H2}$) for lower $AR$ and $\beta_{v1}Kn$, and an increase in temperature jump (decrease in $Nu_{H2}$) for higher $AR$ and $\beta_{v1}Kn$, compared to first-order boundary condition data, when $\beta \neq 0$; while the second-order Karniadakis and Beskok boundary conditions predict an increase in temperature jump (decrease in $Nu_{H2}$) for lower $AR$ and $\beta_{v1}Kn$, and a decrease in temperature jump (increase in $Nu_{H2}$) at higher $AR$ and $\beta_{v1}Kn$, compared to first-order boundary condition data, when $\beta \neq 0$.

### 3.2. Creep flow effects

The effect of creep flow on fully developed $Po/Po_o$ and $Nu/Nu_o$ is presented in Figs. 5 and 6, respectively, for creep velocity to mean velocity ratios, $u_c/u_m$, of $-0.25$, 0.00, and 0.25, and for $AR = 1$, 2, 5, and $\infty$. For these data first-order slip boundary conditions are used, $Pe = 0.5$, and viscous dissipation effects are neglected. $Nu_T$ data are not presented, as creep flow is negligible for thermally fully developed constant wall temperature boundary conditions. Also, because creep flow is zero at $Kn = 0.00$, creep flow effects on $Po/Po_o$ and $Nu/Nu_o$ are not presented for $\beta_{v1}Kn$ less than 0.01. Positive $u_c/u_m$, creep flow in the same direction as the mean flow, is the result of heating; while negative $u_c/u_m$, creep flow in the opposite direction of the mean flow, is the result of cooling.

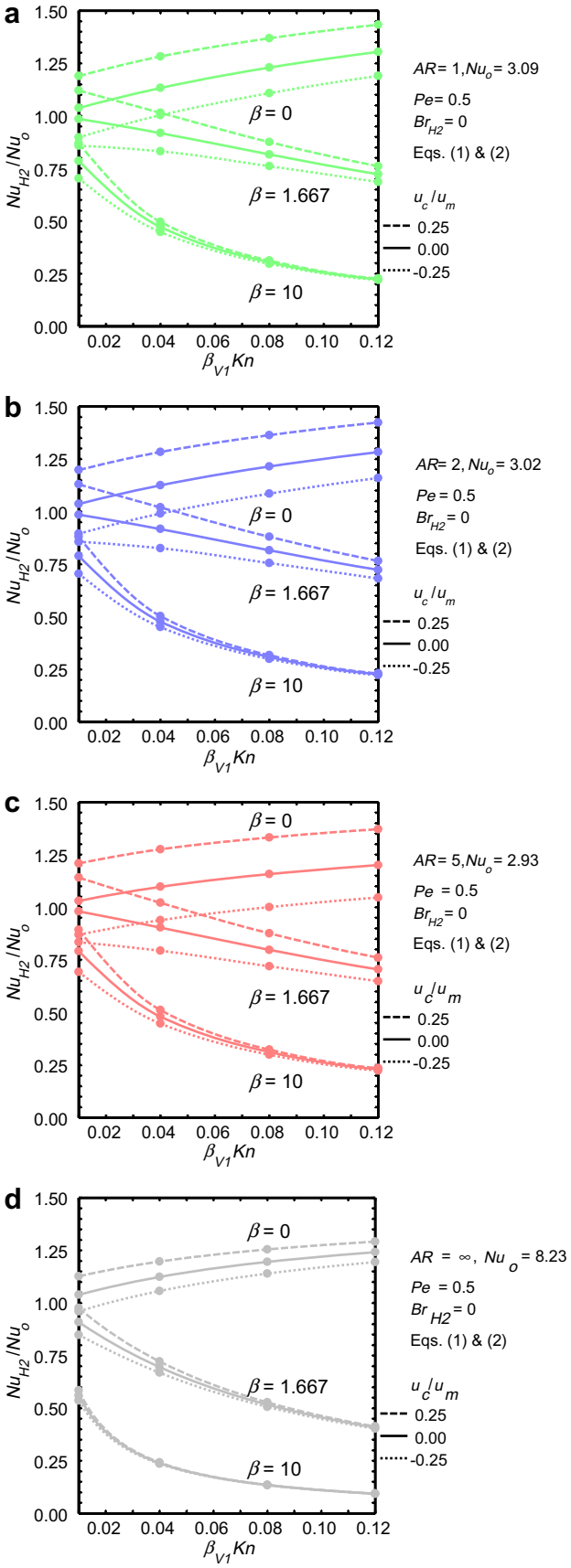


**Fig. 6.** Effect of creep flow on fully developed $Nu_{H2}/Nu_o$: (a) $AR = 1$, (b) $AR = 2$, (c) $AR = 5$, (d) $AR = \infty$.

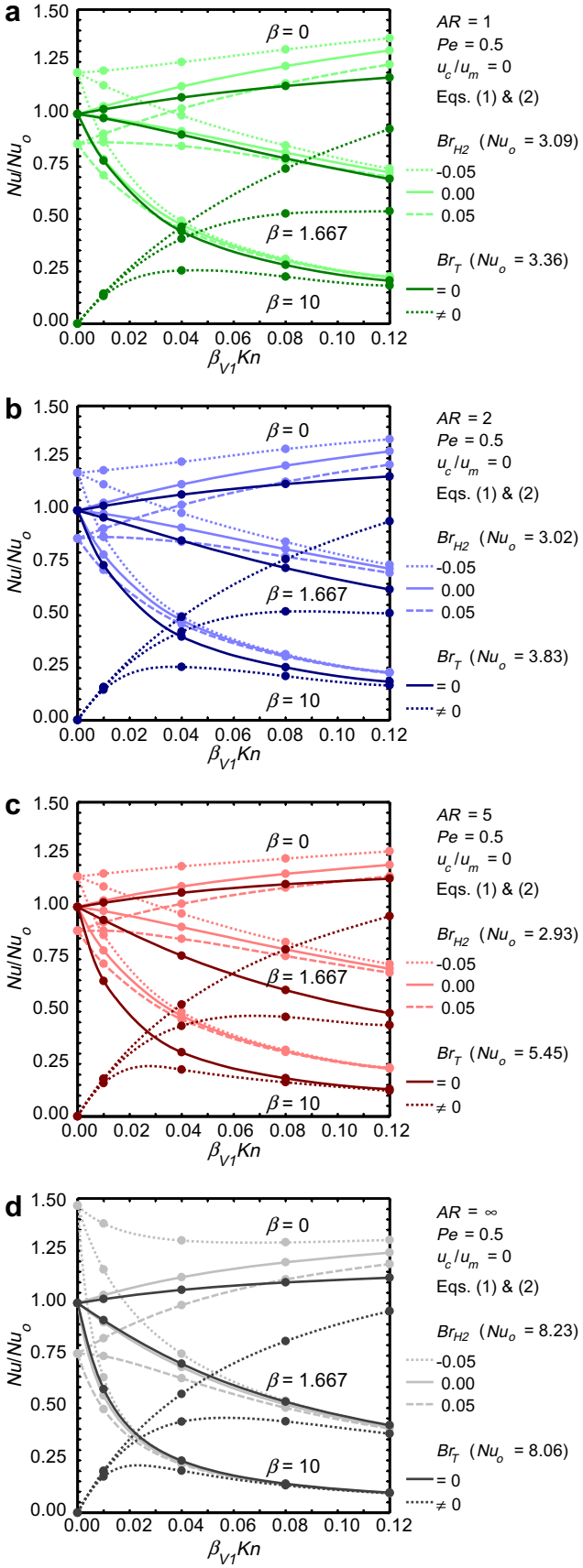


**Fig. 7.** Effect of viscous dissipation on fully developed $Nu/Nu_o$: (a) $AR = 1$, (b) $AR = 2$, (c) $AR = 5$, (d) $AR = \infty$.

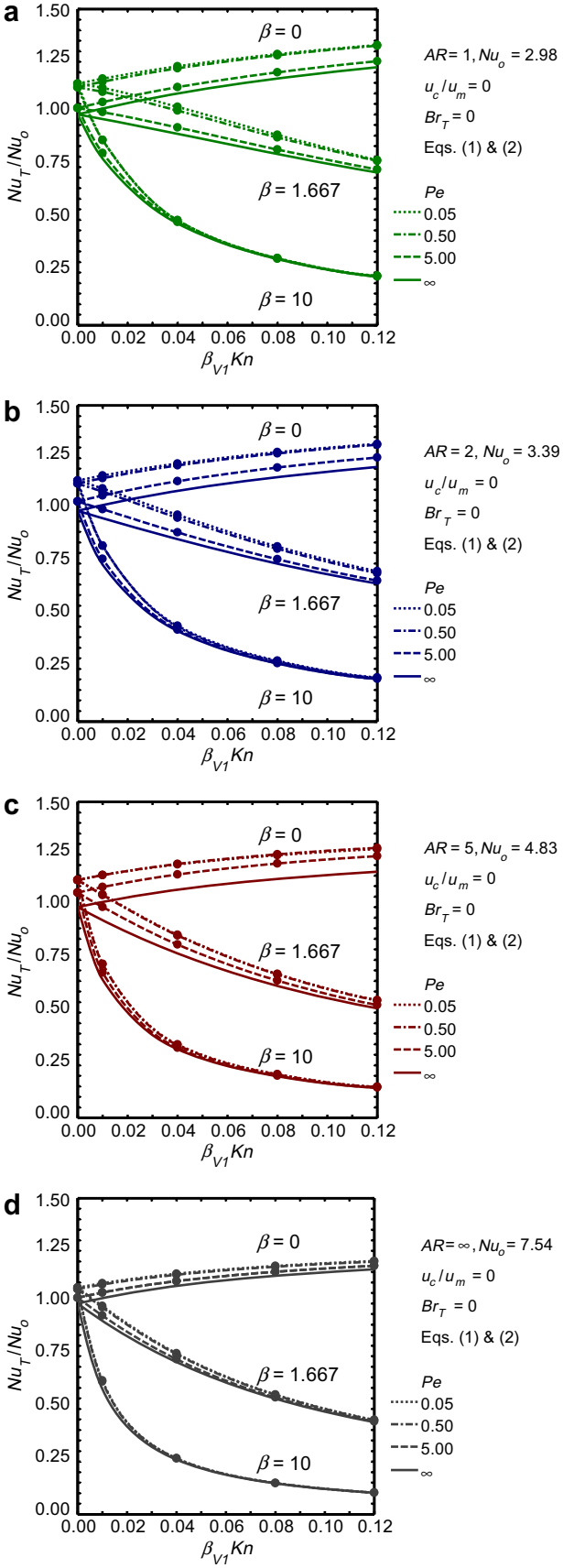


**Fig. 8.** Effect of axial conduction on fully developed $Nu_T/Nu_o$: (a) $AR = 1$, (b) $AR = 2$, (c) $AR = 5$, (d) $AR = \infty$.

The data in Fig. 5 demonstrate that in addition to the $AR$ and $\beta_{v1}Kn$ effects previously discussed, positive $u_c/u_m$, heating, decreases $Po/Po_o$ for all $AR$, while negative $u_c/u_m$, cooling, increases $Po/Po_o$ for all $AR$. Positive $u_c/u_m$ increases the total slip velocity, which decreases the average wall shear stress and reduces $Po/Po_o$. Conversely, negative $u_c/u_m$ decreases the total slip velocity at the wall which increases the average wall shear stress, thereby increasing $Po/Po_o$. Also, because positive $u_c/u_m$ reduces the average wall shear stress there is less of a decrease in $Po/Po_o$ with $\beta_{v1}Kn$, and because negative $u_c/u_m$ increases the average wall shear stress there is more of a decrease in $Po/Po_o$ with $\beta_{v1}Kn$.

There are several factors that contribute to the creep flow effect on $Nu_{H2}$, as presented in Fig. 6. Creep flow in the same direction as the mean flow, heating, increases the total slip velocity, which increases the energy exchange near the wall and tends to increase $Nu_{H2}$. Creep flow in the opposite direction of the mean flow, cooling, decreases the total slip velocity, which decreases the energy exchange near the wall and tends to decrease $Nu_{H2}$. However, as rarefaction increases, the effect of the increasing temperature jump at the wall, for $\beta \neq 0$, and decreasing velocity gradients decrease the energy exchange, which increases the mean temperature difference $(T_w - T_m)$ and reduces $Nu_{H2}$, as well as the effect of $u_c/u_m$ on $Nu_{H2}$. Although $Nu_{H2}$ for $AR = \infty$ follows the same general trends as $Nu_{H2}$ for $AR = 1$, 2, and 5 the effects of creep flow are reduced without the heat flux and creep flow contribution from the two side walls.

### 3.3. Viscous dissipation effects

The effect of viscous dissipation, and the related effects of flow work and shear work, on fully developed $Nu_{H2}$ and $Nu_T$ are given in Fig. 7 for $AR = 1$, 2, 5, and $\infty$. For these data, first-order slip boundary conditions are used, $Pe = 0.5$, and $u_c/u_m = 0$. Because $\mu$ is assumed to be constant, viscous dissipation has no additional effect on $Po/Po_o$. The $Po/Po_o$ data corresponding to the data in Fig. 7 are the same as that given in Fig. 3 for first-order slip boundary conditions. The $Nu_{H2}$ and $Nu_T$ data presented in Fig. 7 are a result of the combined effects of rarefaction $(\beta_{v1}Kn)$, the gas–wall interactions $(\beta)$, and viscous dissipation, flow work, and shear work $(Br)$. Viscous dissipation acts as a distributed heat source, with the majority of the thermal energy generated near the wall, due to the larger velocity gradients. Flow work acts as a distributed heat sink, with the majority of the thermal energy absorbed near the center of the flow, due to the larger velocity magnitudes. And, shear work, $u\partial\tau/\partial y|_{y=0}$, acts as a heat source at the wall, due to the thermal energy generated by the slipping flow.

The $Nu_{H2}$ data in Fig. 7 demonstrate that in addition to the $AR$ and $\beta_{v1}Kn$ effects discussed previously, positive $Br_{H2}$, heating, decreases $Nu_{H2}$, and negative $Br_{H2}$, cooling, increases $Nu_{H2}$. This is because viscous dissipation results in an increase in the fluid temperature at the wall, which for heating, increases the difference between the mixed mean fluid temperature and the average wall temperature, thereby reducing $Nu_{H2}$; while for cooling, this decreases the difference between the mixed mean fluid temperature and the average wall temperature, thereby increasing $Nu_{H2}$. For the constant wall heat flux boundary condition, flow work decreases the wall temperature and the mixed mean fluid temperature by equal amounts, and consequently $Nu_{H2}$ is unaffected by the flow work contribution [40]. The data in Fig. 7 also indicate that the effect of viscous dissipation is reduced for increasing rarefaction. The reduced effect of $Br_{H2}$ on $Nu_{H2}$ with increasing $\beta_{v1}Kn$ is due to the reduced velocity gradients caused by increasing slip at the wall. Although trends in $Nu_{H2}$ due to viscous dissipation and rarefaction are the same for all $AR$ investigated, these effects are more significant for $AR = \infty$ than for $AR = 1$, 2, and 5. This is because the parallel plate channel has larger velocity gradients, resulting in increased viscous dissipation, and with no side wall heat flux contribution the thermal energy generated by viscous dissipation is relatively more significant.

The $Nu_T$ data presented in Fig. 7 with viscous dissipation effects, $Br_T \neq 0$ were obtained for $Pe = 0.5$ and $Br_T = -0.2$. However, as will be explained, for a given $\beta_{v1}Kn$, $\beta$, $AR$, and slip boundary condition model, all flows with viscous dissipation and flow work result in the same fully developed value of $Nu_T$, regardless of the magnitude of $Pe$ or $Br_T$. For fully developed continuum flow, the thermal energy generated by viscous dissipation, is equal to the thermal energy absorbed by flow work. This energy balance results in $\partial T_m/\partial x = 0$, a net wall heat flux of zero, and therefore $Nu_T = 0$, as discussed by [40,27]. Within the slip flow regime, the slip flow at the wall reduces the average cross sectional velocity gradients as well as the maximum core velocity. Although this results in a decrease in both the thermal energy generated by viscous dissipation, and the thermal energy absorbed by flow work, the decrease in viscous dissipation is more significant. The difference, however, is exactly equal to the thermal energy generated by shear work at the wall by the slipping flow - meaning that, for a given velocity profile (which depends on $\beta_{v1}Kn$ and $AR$), viscous dissipation, flow work, and shear work are still balanced energy sources and sinks, i.e. $\partial T_m/\partial x = 0$, regardless of the magnitude of $Br_T$ or $Pe$ [20]. However, the shear work at the wall creates a nonzero wall heat flux and therefore a nonzero $Nu_T$. The shear work, $u\partial\tau/\partial y|_{y=0}$, is a function of both the slip velocity and the wall normal velocity gradients. As $\beta_{v1}Kn$ increases, the slip velocity increases, and for the lower slip flow regime this increases the shear work and therefore increases $Nu_T$. However, as the slip velocity increases the velocity gradients throughout the flow decrease, and for the upper end of the slip regime this leads to a decrease in the shear work. These effects, combined with the effect of $AR$ and temperature jump $(\beta \neq 0)$, which, decreases the energy exchange at the wall with increasing $\beta_{v1}Kn$, result in the $Nu_T$ trends displayed in Fig. 7.

### 3.4. Axial conduction effects

Fully developed, slip flow $Nu_T$, computed using $Pe = 0.05$, 0.50, and 5.0, are presented in Fig. 8 for $AR = \infty$, 5, 2, and 1. Using the present compressible flow algorithm, $Nu_T$ can not be computed at large $Pe$ without introducing variation due to compressibility. For this reason, $Nu_T$ presented at $Pe = \infty$ are the analytic solutions of [29], for which compressibility and axial conduction effects have been neglected. $Nu_{H2}$ data are not presented, as axial conduction effects are negligible for thermally fully developed constant wall heat flux boundary conditions. Again, because $\mu$ is assumed to be constant, axial conduction has no additional effect on $Po/Po_o$. The $Po/Po_o$ data corresponding to the data in Fig. 8 are the same as that given in Fig. 3 for first-order slip boundary conditions.

For continuum flow, $\beta_{v1}Kn = 0$, the trends of the $Nu(Pe)$ data presented in Fig. 8, for rectangular microchannels, are consistent with those previously presented for parallel plate channels in Table 2. These results indicate that axial conduction effects become significant as $Pe$ decreases, and result in an increase in $Nu_T$. For the range of $Pe$ investigated, the average absolute change in $Nu_T$, is 0.53, for continuum flow. This is equivalent to 7.6% and 15.0% differences, for parallel plate and square channel flows, respectively. $Nu_T$ decreases considerably, approximately 60% of the overall change, from $Pe = 0.5$ to $Pe = 5.0$. This result is expected, as the thermal energy exchange transitions from being dominated by axial conduction, $Pe < 1$, to convection, $Pe > 1$.

The numerical data in the slip flow regime, are consistent with the trends and magnitudes of the data without axial conduction

$Nu_T$ increases with $AR$, and may increase or decrease with $\beta_{v1}Kn$ depending on $\beta$. The data in Fig. 8 illustrate that for decreasing $Pe$, axial conduction effects increase $Nu_T$, however this effect is reduced as $\beta_{v1}Kn$ increases. The reduced axial conduction effects correspond to increased convection at the walls caused by the slip velocity for increasing $\beta_{v1}Kn$, and the decrease in the total energy exchange due to the temperature jump, for $\beta \neq 0$.

## 4. Summary and conclusions

The Poiseuille and Nusselt numbers for rectangular microchannels with both constant wall heat flux and constant wall temperature thermal boundary conditions in the slip regime have been numerically calculated. The resulting $Po$, $Nu_{H2}$, and $Nu_T$ include the effects of second-order velocity slip and temperature jump boundary conditions, creep flow, and viscous dissipation with flow work. The numerical results for $Po$, $Nu_{H2}$, and $Nu_T$ are presented in terms of the degree of rarefaction ($\beta_{v1}Kn$); the gas–wall interaction parameter ($\beta$); creep flow ($u_c/u_m$); viscous dissipation ($Br_{H2}$ or $Br_T$); and axial conduction ($Pe$). These results are valid for incompressible or nearly incompressible, locally fully developed, steady state flows. The numerical solutions for microchannel $Po$, $Nu_{H2}$, and $Nu_T$ have been calculated using a continuum based three-dimensional, unsteady, compressible, CFD algorithm modified with slip boundary conditions.

The results of this study indicate that the effects of second-order slip boundary conditions, creep flow, viscous dissipation with flow work, and axial conduction are all significant within the slip flow regime for rectangular microchannel pressure losses and convective heat transfer rates. The significance of each of these terms depends on the degree of rarefaction, the gas–wall interactions, and the thermal boundary conditions. Effects of second-order boundary conditions increase as rarefaction increases, with the two models studied having opposite effects when compared to first-order boundary conditions. The accuracy of solutions generated with the second-order boundary conditions requires comparison with experimental data, which does not currently exist. Creep flow results in an increase in $Nu_{H2}$ for heating and decrease in $Nu_{H2}$ for cooling by an amount dependant on $u_c/u_m$, $\beta_{v1}Kn$, $\beta$, and $AR$. The effects of creep flow, for a given $u_c/u_m$, are decreased with increasing $\beta_{v1}Kn$. Viscous dissipation increases $Nu_{H2}$ for cooling and decreases $Nu_{H2}$ for heating as a function of $Br_{H2}$, $\beta_{v1}Kn$, $\beta$, and $AR$. The combined effects of viscous dissipation, flow work, and shear work within the slip flow regime cause $Nu_T$ to increase with increasing $\beta_{v1}Kn$, by an amount dependent on $AR$ and $\beta$, but independent of $Br_T$ and $Pe$. Axial conduction effects are significant for flow with low Peclet number, and may increase the Nusselt number by up to 15%, for the aspect ratios studied, compared to $Nu_T$ without axial conduction effects. Effects of axial conduction increase with decreasing $Pe$, and are decreased with increasing $\beta_{v1}Kn$.

## Acknowledgements

Partial support of this work by National Science Foundation Grant No. DGE9987616, of the Integrative Graduate Education and Research Traineeship Program, and US Department of Energy Grant No. W-7405-ENG-48, through the Center for the Simulation of Accidental Fires and Explosions, is gratefully acknowledged.

## References

[1] G.E. Karniadakis, A. Beskok, Micro Flows: Fundamentals and Simulation, Springer-Verlag, New York, 2002.
[2] J.C. Maxwell, On stresses in rarified gases arising from inequalities of temperature, Philos. Trans. R Soc. Lond. 170 (1879) 231–256.
[3] M. Smoluchowski, Ueber wärmeleitung in verdünnten gasen, Annal. Phys. Chem. 64 (1898) 101–130.
[4] R.G. Deissler, An analysis of second-order slip flow and temperature-jump boundary conditions for rarefied gases, Int. J. Heat Mass Transfer 7 (1964) 681–694.
[5] J. Dai, D. Xu, C. Khoo Boo, Y. Lam Khin, Navier–Stokes simulation of gas flow in micro devices, J. Micromech. Microeng. 10 (2000) 372–379.
[6] J.-M. Li, B.-X. Wang, X.-F. Peng, 'Wall-adjacent layer' analysis for developed-flow laminar heat transfer of gases in microchannels, Int. J. Heat Mass Transfer 43 (2000) 839–847.
[7] H. Xue, Q. Fan, A new analytic solution of the Navier–Stokes equations for microchannel flows, Microscale Thermophys. Eng. 4 (2000) 125–143.
[8] D.A. Lockerby, J.M. Reese, High-resolution Burnett simulations of micro Couette flow and heat transfer, J. Comput. Phys. 188 (2003) 333–347.
[9] M.J. McNenly, M.A. Gallis, I.D. Boyd, Empirical slip and viscosity model performance for microscale gas flow, Int. J. Numerical Methods Fluids 49 (2005) 1169–1191.
[10] J. Maurer, P. Tabeling, P. Joseph, H. Willaime, Second-order slip laws in microchannels for helium and nitrogen, Phys. Fluids 15 (2003) 2613–2621.
[11] S. Colin, P. Lalonde, R. Caen, Validation of a second-order slip flow model in rectangular microchannels, Heat Transfer Eng. 25 (2004) 23–30.
[12] G. An, J.-M. Li, B.-X. Wang, Laminar heat transfer of gas in a parallel-plate microchannel with one wall temperature constant and the other adiabatic, Heat Transfer – Asian Res. 32 (2003) 58–64.
[13] C.o.-K. Chen, H.C. Weng, Developing natural convection with thermal creep in a vertical microchannel, J. Phys. D: Appl. Phys. 39 (2006) 3107–3118.
[14] J.N. Chung, J. Yan, Y. Kun, Numerical simulation of wall roughness on gaseous flow and heat transfer in a microchannel, Int. J. Heat Mass Transfer 49 (2006) 1329–1339.
[15] N. Xiao, J. Elsnab, S. Thomas, T. Ameel, Isothermal microtube heat transfer with second-order slip flow and temperature jump boundary conditions, in: Proceedings of 2006 ASME International Mechanical Engineering Congress and Exposition IMECE2006, Chicago, IL, United States, 2006, p. 9.
[16] X. Zhu, Q. Liao, M.D. Xin, Gas flow in microchannel of arbitrary shape in slip flow regime, Microscale Thermophys. Eng. 10 (2006) 41–54.
[17] J. van Rij, T. Harman, T. Ameel, The effect of creep flow on two-dimensional isoflux microchannels, Int. J. Thermal Sci. 46 (2007) 1095–1103.
[18] G. Tunc, Y. Bayazitoglu, Heat transfer in microtubes with viscous dissipation, Int. J. Heat Mass Transfer 44 (2001) 2395–2403.
[19] G. Tunc, Y. Bayazitoglu, Heat transfer in rectangular microchannels, Int. J. Heat Mass Transfer 45 (2002) 765–773.
[20] N.G. Hadjiconstantinou, Dissipation in small scale gaseous flows, J. Heat Transfer 125 (2003) 944–947.
[21] O. Aydin, M. Avci, Analysis of micro-Graetz problem in a microtube, Nanoscale Microscale Thermophys. Eng. 10 (2006) 345–358.
[22] O. Aydin, M. Avci, Thermally developing flow in microchannels, J. Thermophys. Heat Transfer 20 (2006) 628–632.
[23] T.N. Aynur, L. Kuddusi, N. Egrican, Viscous dissipation effect on heat transfer characteristics of rectangular microchannels under slip flow regime and H1 boundary conditions, Heat Mass Transfer/Waerme Stoffuebertragung 42 (2006) 1093–1101.
[24] C.-H. Chen, Slip-flow heat transfer in a microchannel with viscous dissipation, Heat Mass Transfer/Waerme Stoffuebertragung 42 (2006) 853–860.
[25] H.-E. Jeong, J.-T. Jeong, Extended Graetz problem including streamwise conduction and viscous dissipation in microchannel, Int. J. Heat Mass Transfer 49 (2006) 2151–2157.
[26] W. Sun, S. Kakac, A.G. Yazicioglu, A numerical study of single-phase convective heat transfer in microtubes for slip flow, Int. J. Thermal Sci. 46 (2007) 1084–1094.
[27] R.K. Shah, A.L. London, Laminar Flow Forced Convection in Ducts, Academic Press, New York, 1978 (Chapters 6 and 7).
[28] F. Yan, B. Farouk, Computations of low pressure fluid flow and heat transfer in ducts using the direct simulation Monte Carlo method, J. Heat Transfer 124 (2002) 609–616.
[29] S. Yu, Slip Flow Heat Transfer in Rectangular Microchannels, Ph.D. thesis, University of Utah, Salt Lake City, Utah, 2002.
[30] M. Renksizbulut, H. Niazmand, G. Tercan, Slip-flow and heat transfer in rectangular microchannels with constant wall temperature, Int. J. Thermal Sci. 45 (2006) 870–881.
[31] J. van Rij, T. Ameel, T. Harman, The effect of viscous dissipation on two-dimensional microchannel heat transfer, in: Proceedings of 2006 ASME International Mechanical Engineering Congress and Exposition IMECE2006, Chicago, IL, United States, 2006, p. 9.
[32] J. van Rij, T. Ameel, T. Harman, Constant wall temperature Nusselt and Poiseuille numbers in rectangular microchannels, in: Proceedings of 2007 ASME-JSME Thermal Engineering Summer Heat Transfer Conference HT2007, Vancouver, BC, Canada, 2007, pp. 893–900.
[33] J. van Rij, T. Ameel, T. Harman, Effects of creep flow and viscous dissipation in the slip regime for isoflux rectangular microchannels, in: Proceedings of 2007 ASME International Mechanical Engineering Congress and Exposition IMECE2007, Seattle, WA, United States, 2007, pp. 971–978.
[34] B.A. Kashiwa, N.T. Padial, R.M. Rauenzahn, W.B. VanderHeyden, A Cell-Centered Ice Method for Multiphase Flow Simulations, Los Alamos National Laboratory Technical Report LA-UR-93-3922, 1993.

[35] B.A. Kashiwa, A Multifield Model and Method for Fluid–Structure Interaction Dynamics, Los Alamos National Laboratory Technical Report LA-UR-01-1136, 2001.
[36] S.G. Parker, J. Guilkey, T. Harman, A component-based parallel infrastructure for the simulation of fluid–structure interaction, Eng. Comput. 22 (2006) 277–292.
[37] J.E. Guilkey, T.B. Harman, B. Banerjee, An Eulerian–Lagrangian approach for simulating explosions of energetic devices, Comput. Struct. 85 (2007) 660–674.
[38] M. Spiga, G.L. Morini, Nusselt numbers in laminar flow for H2 boundary conditions, Int. J. Heat Mass Transfer 39 (1996) 1165–1174.
[39] W.A. Ebert, E.M. Sparrow, Slip flow in rectangular and annular ducts, J. Basic Eng. (1965) 1018–1024.
[40] J.W. Ou, K.C. Cheng, Effects of flow work and viscous dissipation on Graetz problem for gas flows in parallel-plate channels, Heat Mass Transfer 6 (1973) 191–198.